Deep ocean wave energy conversion using a cycloidal turbine

S.G. Siegel *, T. Jeans, T.E. McLaughlin

Department of Aerospace Engineering, 2410 Faculty Drive, US Air Force Academy, CO, 81001, USA

ARTICLE INFO

ABSTRACT

A lift based wave energy converter, namely, a cycloidal turbine, is investigated. This type of wave energy converter consists of a shaft with one or more hydrofoils attached eccentrically at a radius. The main shaft is aligned parallel to the wave crests and submerged at a fixed depth. In the two-dimensional limit, i.e. for large spans of the hydrofoil (or an array of these), the geometry of the converter is suitable for wave termination of straight crested Airy waves. Results from two-dimensional potential flow simulations, with thin hydrofoils modeled as either a point vortex or discrete vortex panel, are presented. The operation of the cycloidal turbine both as a wave generator as well as a wave-to-shaft energy converter interacting with a linear Airy wave is demonstrated. The impact on the performance of the converter for design parameters such as device size, submergence depth, and number of hydrofoils is shown. For optimal parameter choices, simulation results demonstrate inviscid energy conversion efficiencies of more than 99% of the incoming wave energy to shaft energy. This is achieved using feedback control to synchronize the rotational rate, blade pitch angle, and phase of the cycloidal wave energy converter to the incoming wave. While complete termination of the incoming wave is shown, the remainder of the energy is lost to harmonic waves traveling in the up-wave and down-wave directions.

1. Introduction

Among alternative energy sources, wave power is one of the most abundant sources on Earth. The World Energy Council, according to Boyle [1], has estimated the world wide annual amount of wave power energy at 17.5 PWh (Peta Watt hours = 10^{12} kWh). This is comparable to annual world wide electric energy consumption, which is currently estimated at 16 PWh. Thus, wave power has the potential to provide a large portion of the world's electric energy needs if it can be tapped efficiently. Other advantages of wave power include its power density, predictability, and location. While the power density of both solar and wind power in typical favorable sites is of the order of 1 kW m^{-2} according to Bedart [2], wave power in a typical North Atlantic wave as considered in this paper (wave height of $H = 3.5$ m and period of $T = 9$ s) yields 108 kW m^{-1} of wave crest. As will be shown, a device extending about 40 m in the vertical direction can extract almost all of this wave power, yielding a power density of about 2.7 kW m^{-2}, or more than twice that of wind or solar power. If one considers the theoretical inviscid conversion limits for waves and wind, which are 100% for waves [3] and 59% for wind [4], the accessible power densities of waves and wind differ by a factor of more than 4. Furthermore, wave energy is available on a more consistent basis and can be better predicted in advance, reducing the need for conventional back up power sources. Finally, since a large portion of the world's population lives close to ocean shores, the distance between energy production and consumption is small, reducing transmission losses. Thus, wave power is an ideal energy source for efficiently providing renewable energy to densely populated coastal areas.

Given the attractive features of wave energy as an alternative energy source, it has received significant attention in the scientific community over recent times. While a comprehensive review of all relevant publications would be prohibitively long, the reader is instead referred to comprehensive reviews published by McCormick [5], Mei [6] or, most recently, Cruz [7]. The following discussion will instead focus only on select sources most pertinent to the current work.

Relatively few publications investigate the interaction of hydrofoils with surface waves for the purpose of wave energy conversion. Wu [8] analyzed the interaction of an oscillating hydrofoil with waves. He identified by means of variational calculus optimal oscillating parameters and reported that a net energy gain can be obtained. Grue et al. [9] explored the possibility of using energy recovered from waves using an oscillating hydrofoil as a means of propulsion for a vessel. They investigated the possible parameter space in detail using linearized potential flow simulations, and found that, in particular for waves traveling in the opposite direction to the vessel, a large amount of propulsion energy can be extracted from the waves. This concept was further pursued by Isshiki [10], Isshiki and Murakami [11] and Isshiki et al. [12], resulting in a vessel crossing the Pacific Ocean from Japan to the island of Hawaii entirely powered by wave energy [13].

* Corresponding author. Tel.: +1 719 333 9080.
E-mail address: stefan@siegels.us (S.G. Siegel).

More specifically, for the application of alternative energy, initial investigations of lift based wave energy conversion by means of a single hydrofoil were performed at TU Delft as early as the 1990s, both experimentally by Marburg [14] and numerically by van Sabben [15]. As noted by Hermans et al. [16], a major advantage of this approach over traditional wave energy converters is that the wave energy can be converted directly into rotational mechanical energy. This initial work demonstrated the feasibility of the approach, as well as the ability of a cycloidal wave energy converter (WEC) to self-synchronize with the incoming wave in terms of rotational phase. However, the conversion efficiencies found both in the theoretical work and the wave tunnel experiments conducted at TU Delft were very small, of the order of few percent in experiments, with a theoretical maximum of 15%. Pinkster and Hermans [17] also demonstrated the use of a cycloidal propeller as a means of detecting wave direction and period with good accuracy.

The aim of the present work is to extend the numerical work of Hermans et al. [16] and Pinkster and Hermans [17] to investigate the performance improvements of a cycloidal WEC that operates at significantly higher blade speeds then the wave-induced velocity. The impact of all geometric design parameters in terms of the far-field wave generation and cancellation is explored. Near-field investigations are used to investigate the impact of different blade pitch control schemes as well as hydrofoil chord length on energy conversion efficiency. Additional efficiency improvements using a multi-bladed converter with positive harmonic wave interactions are also investigated.

1.1. Wave energy converter geometry

A typical cycloidal WEC, as considered in this paper, is shown in Fig. 1. It features one or more hydrofoils attached parallel to a horizontally oriented main shaft at a radius R, rotating clockwise at angular speed ω, and submerged a depth y_c, which is measured relative to a Cartesian coordinate system with $y = 0$ being the undisturbed free surface. The hydrofoils in the 2D simulations in this paper are assumed to have infinite span in the third dimension, which in real life can be approximated by having a large aspect ratio, which is the ratio between chord length and span. They are also assumed to be aligned parallel with the incident wave crests. The orientation (pitch) of each hydrofoil may be adjusted to produce the desired level of circulation Γ. At any point on the free surface the vertical elevation is η and peak-to-peak amplitude of the resulting wave field is H. The incoming ocean wave W_{Airy}, is assumed to travel left to right, and waves generated by the cycloidal WEC traveling in the direction of the incoming wave receive a positive index (e.g., W_1) and are considered as traveling down-wave; while waves traveling in the opposite direction are considered as traveling up-wave and receive a negative index (e.g., W_{-1}).

2. Potential flow model

Since a typical wave-induced flow field is well described by potential flow theory, see for example [18], a logical starting point to investigate the wave making and cancellation properties of a cycloidal WEC is to seek a potential flow solution. For an inviscid, incompressible, and irrotational flow, the governing continuity equation simplifies to the Laplace equation

$$\nabla^2 \Phi = 0, \tag{1}$$

where Φ is the velocity potential. Unique solutions to Eq. (1) are determined by satisfying the appropriate boundary conditions based on physical considerations. In seeking two-dimensional
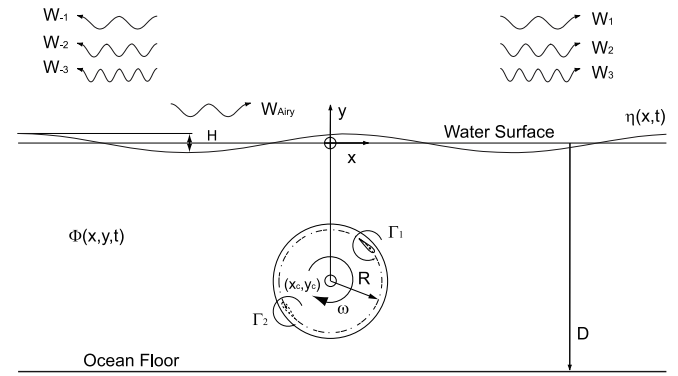

Fig. 1. Cycloidal wave energy converter geometry.

solutions it is often convenient to define the complex stream function in terms of the complex coordinate $z = x + iy$,

$$F(z, t) = \Phi + i\Psi, \tag{2}$$

where Ψ is the stream function and the complex velocity is defined by $dF/dz = u - iv$.

2.1. Point vortex model

The simplest representation of a two-dimensional hydrofoil correctly representing the flow induced in the far-field is a point vortex of strength Γ equal to the foil circulation. If the vortex is in the presence of a free surface it is imperative that appropriate physical boundary conditions be satisfied on the free surface. Derivations of the linearized free surface boundary condition can be found, for example, in [18]. Neglecting higher order terms, the kinematic boundary condition ensuring the vertical velocity of the free surface and the fluid are equal is

$$\frac{\partial \eta}{\partial t} = \frac{\partial \Phi}{\partial y}. \tag{3}$$

The dynamic boundary condition ensuring the pressure on the free surface is atmospheric is determined from Bernoulli's equation. Substituting the free surface elevation for y, and again neglecting higher order terms results in

$$\eta = -1/g \frac{\partial \Phi}{\partial t}, \tag{4}$$

where $g = 9.81 \text{ ms}^{-2}$ is the gravity constant. Due to the linearization, Eq. (4) can be imposed at $y = 0$. At the up-wave and down-wave integration boundaries, the waves within the domain are allowed to leave the domain freely using a non-reflective boundary condition.

Subject to the above boundary condition, the complex potential for a vortex moving under a free surface with position $c(t) = x(t) + iy(t)$ in the complex plane is developed in [19] to be

$$F(z, t) = \frac{\Gamma(t)}{2\pi i} \ln\left(\frac{z - c(t)}{z - \bar{c}(t)}\right) + \frac{g}{\pi i} \int_0^t \int_0^\infty \frac{\Gamma(\tau)}{\sqrt{gk}} e^{-ik(z - \bar{c}(\tau))}$$
$$\times \sin[\sqrt{gk}(t - \tau)] dk d\tau \tag{5}$$

with $\Gamma(t)$ the circulation of the vortex, and k the wave number. Eq. (5) satisfies both the kinematic and dynamic free surface boundary conditions at $y = 0$. The first term is the complex potential due to the vortex and its mirror image above the surface, which is necessary to satisfy the kinematic free surface condition. The second term describes the radiated waves related to the dynamic free surface condition. It is also important to note that in Eq. (5) the fluid is assumed to be infinitely deep. While the

circulation $\Gamma(t)$ can be described in a time dependent fashion, it constitutes a numerical model of limited capabilities in terms of correctly representing an unsteady hydrofoil of time varying angle of attack. This is because an actual hydrofoil would shed vorticity into its wake of an amount equal to the change in circulation, and this is not accounted for in Eq. (5).

In previous work by Hermans et al. [16] and Pinkster and Hermans [17] a hydrofoil under a free surface was modeled by numerically integrating Eq. (5) and the results were compared to steady flow experiments with good agreement. A similar approach is employed in the current work and Eq. (5) is integrated using second order time and wave number marching techniques. Subsequently, Eq. (4) is used to determine the resulting surface elevation and wave pattern. Using superposition, this approach is further extended to a WEC with multiple hydrofoils, where the complex potential of each hydrofoil is represented by Eq. (5). The total potential is determined from $\Phi_{total} = \sum_{i=1}^{n} \Phi_i$, where n is the total number of hydrofoils.

For all single vortex simulations the position of the vortex is prescribed as a function of time. The coordinates for the vortex moving about the center of rotation $(0, y_c)$ with radius R and frequency ω are

$$x(t) = R\cos(\omega t + \theta)$$
$$y(t) = y_c - R\sin(\omega t + \theta). \tag{6}$$

Thus, the motion of the converter starts with the first (or sole) blade being in the most down-wave position, and rotation is in the clockwise direction as shown in Fig. 1. The WEC is assumed synchronized with the incoming Airy wave such that $\omega = \omega_{Airy}$. An arbitrary phase shift θ is introduced, which indicates the relative phase between an incoming wave and the cycloidal WEC motion.

2.2. Thin hydrofoil model

The singularity of a single point vortex does not represent a hydrofoil well in the near-field, and therefore it is impossible to determine important near-field quantities like angle of attack using the approach outlilned in Section 2.1. In order to analyze the near-field, one must resort to a thin hydrofoil panel representation.

The vortex panel representation employed follows the algorithm for an unsteady thin airfoil using the lumped-vortex element method described by Katz and Plotkin [20] Chapter 13.10 with modifications to account for the free surface. The governing continuity equation for the incompressible unsteady flow field in a body-fixed coordinate system is still represented by Eq. (1) at any point in time. Thus, a time marching scheme can be implemented with unsteadiness entering the problem via the hydrofoil surface boundary condition and wake.

The hydrofoil is divided into a finite number of panels and a discrete vortex is located at the quarter chord of each panel. A Neumann boundary condition satisfying no flow penetration through the hydrofoil surface is satisfied at three-quarters chord of each panel, according to

$$(\nabla\Phi_B + \nabla\Phi_W + \nabla\Phi_{Airy} - \mathbf{V}_0 - \boldsymbol{\Omega} \times \mathbf{r}) \cdot \mathbf{n} = \mathbf{0}, \tag{7}$$

where Φ_B is the self-induced perturbation potential, Φ_W is the wake potential, Φ_{Airy} is the potential due to the incoming Airy wave, $\mathbf{V}_0$ is the velocity of the body-fixed origin, $\mathbf{r}$ is the body-fixed position vector, and $\boldsymbol{\Omega}$ is the rate of rotation in the body-fixed coordinate system. Each discrete vortex represented in Φ_B and Φ_W is modeled using Eq. (5), ensuring that the free surface boundary conditions of Eqs. (3) and (4) are satisfied. Note that for the discrete vortex model the instantaneous Kutta condition is satisfied implicitly.

At each time step a discrete vortex is added to the hydrofoil wake such that Kelvin's condition is satisfied. As recommended

by Katz and Plotkin [20], the vortex is placed along the path of the hydrofoil's trailing edge at approximately $0.25l$ from the trail edge, where l is the distance traveled within the time step. Each wake vortex is considered force free and within each time step is convected by the local velocity, which includes velocity components induced by the wake, hydrofoil, and incoming Airy wave. No dissipation of vorticity over time was considered, and there was no need to implement any vortex core models as the integration scheme proved stable without them.

The hydrofoil motion is prescribed as a function of time, with the trajectory of the body-fixed coordinate system located at the hydrofoil nose defined by Eq. (6). The hydrofoil is also free to pitch about the body-fixed orgin by an angle α, which is either prescribed or determined iteratively at each time step such that a specified circulation is achieved.

2.3. Incoming Airy wave

Linear Airy wave theory is used to investigate the interaction of the cycloidal WEC and the incoming wave. The velocity potential for a progressive linear deep ocean wave satisfying the linearized free surface boundary conditions is given in [18] to be

$$\Phi_{Airy}(x, y, t) = \frac{Hg}{2\omega}e^{ky}\sin(kx - \omega t), \tag{8}$$

where H is the peak-to-peak wave amplitude, ω is the wave frequency and k is the wave number. Superposition is again utilized to determine the total velocity potential.

Airy wave theory can also be used to describe the phase speed C, group velocity C_g, wavelength λ_{Airy}, and wave period T, such that

$$C = g\frac{T_{Airy}}{2\pi}$$
$$C_g = C/2$$
$$\lambda_{Airy} = CT_{Airy}. \tag{9}$$

Typically, the WEC will create more than a single plane traveling wave. The wave height of each generated wave component can be determined by Fourier analysis. Throughout this paper indices are used to identify the harmonic wave components and their traveling direction. As shown in Fig. 1, waves traveling left or in the up-wave direction receive negative indices, while down-wave traveling waves receive positive indices. It is possible to determine the power associated with each wave P_n by employing Airy wave theory which relates wave power per unit length to wave height and period by

$$P_n = \frac{1}{8}\rho g H_n^2 C_g$$
$$= \frac{1}{32\pi}\rho g^2 H_n^2 T_n, \tag{10}$$

where $\rho = 1000 \text{ kg m}^{-3}$ is the density of water. Since the wave power scales linearly with the wave period T, higher harmonic waves of the same wave height will contain less energy in proportion to their period. Also to be noted is a quadratic relationship between wave energy and wave height H. Based on wave power, the figure of merit for WEC design becomes the ratio of the power in the (desired) fundamental wave traveling down-wave, P_1, compared to the power contained in all waves,

$$P_1/P_{all} = \frac{P_1}{\sum_{n=-\infty}^{\infty} P_n}. \tag{11}$$

The power ratio will reach a value of one if only the desired down-wave traveling fundamental wave is created, and zero if no
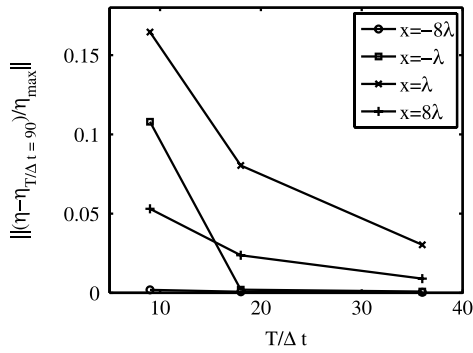
Fig. 2. L2 error norm as a function of time step discretization for $\Delta k/k_{Airy} = 31.6$ and $k_{max}/k_{Airy} = 75.9$.

Fig. 3. Water surface–time plot for wave generation by a single vortex cycloidal WEC with device size $2R/\lambda_{Airy} = 0.3$, submergence depth $|y_c|/\lambda_{Airy} = 0.18$, and circulation $\Gamma T/\lambda^2_{Airy} = 5.6 \times 10^{-3}$. The converter is located at $x/\lambda_{Airy} = 0$ and rotation is started at $t/T = 0$.

down-wave traveling fundamental wave is produced. The wave power analysis is based on energy conservation which is implicit in the unsteady Bernoulli equation, and a control volume analysis assuming that all energy leaving or entering at the up-wave and down-wave boundaries is contained in traveling Airy type waves. Thus, the power difference at both boundaries is to be provided or absorbed by the traveling point vortex/vortices.

3. Results

While the actual ocean environment typically consists of waves with several different periods and wave heights superimposed, in this initial investigation a sinusoidal, plane Airy wave is assumed. According to Boyle [1], the North Atlantic often features waves with a period of $T = 9$ s and wave length $\lambda_{Airy} = 126.5$ m (asuming linear Airy wave theory). Based on the sketch in Fig. 1 and the incident Airy wave, a number of non-dimensional quantities emerge. The basic size of the WEC is denoted by $2R/\lambda_{Airy}$, depth of submergence by $|y_c|/\lambda_{Airy}$, hydrofoil chord by c/λ_{Airy} and wave height by H/λ_{Airy}. It is also convenient for parameter studies to compare different-sized WECs while keeping the distance between the water surface and the upper point of the cycloidal WEC trajectory fixed, that is $|y_c + R|/\lambda_{Airy} = const.$

3.1. Convergence study

It is imperative to ensure that the time step and wave number integration settings are such that the numerical solution sufficiently converges. Resulting wave patterns for single vortex simulations were investigated as a function of Δt, Δk, and k_{max} to determine appropriate values for each variable. Fig. 2 presents the L2 error, normalized by the largest down-wave surface elevation η_{max}. Results are shown for fixed axial locations $x/\lambda_{Airy} = -8, -1, 1$, and 8. The effect of varying Δt is shown for constant $\Delta k/k = 31.6$ and $k_{max}/k = 75.9$. These plots show a decreasing error as Δt decreases; also, the errors are larger close to the cycloidal turbine, indicating the need for increased time resolution in this region.

Similar investigations were conducted for the wave number increment Δk, and maximum resolved wave number k_{max}. Based on these results it was concluded that the required resolutions for numerical convergence are $T/\Delta t = 36$, $k/\Delta k = 31.6$, and $k_{max}/k = 75.9$. The results obtained with these integration parameters were compared to a simulation with $T/\Delta t = 72$, $k/\Delta k = 63.2$, and $k_{max}/k = 151.8$, and both simulations predicted nearly identical wave patterns, indicating that the chosen settings are sufficient. These values were employed for all simulations presented, including the thin hydrofoil simulations. Further verification was performed by comparing data presented by Marburg [14] using the same simulation parameters, and identical results were obtained. As a source of validation, Marburg [14] compared single vortex simulation results to wave tunnel experiments conducted at TU Delft and found good agreement.
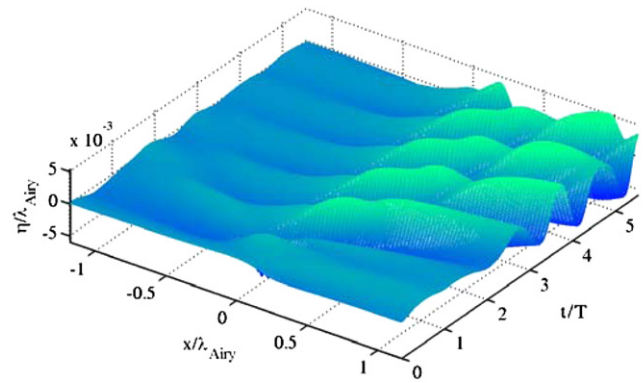
3.2. Point vortex model results

Far field results are presented for simulations with each hydrofoil modeled as a point vortex using the complex potential given in Eq. (5).

3.2.1. Single-blade wave energy converter

Results from single vortex simulations, representing a single-bladed cycloidal WEC, are presented in this section. The goal of these simulations is to investigate the nature of the waves generated by the cycloidal WEC and to determine optimal values for radius R, centroid location beneath the water surface y_c, and circulation Γ. The optimal wave pattern generated by the WEC is one with a fundamental wave traveling down-wave equal in amplitude (but of opposite phase) to the incoming Airy wave, and no higher harmonic waves traveling in the up- or down-wave directions.

Plotted in Fig. 3 is a typical resulting wave pattern as a function of time. The size of the WEC is $2R/\lambda_{Airy} = 0.3$ and the submergence depth is $|y_c|/\lambda_{Airy} = 0.18$, which (as will be shown in a subsequent section) avoids generating excessively large harmonic waves. It can be seen that the dominant wave amplitudes occur in the down-wave direction, while the up-wave amplitudes are small. After several rotations of the WEC the flow becomes periodic in time and space. However, beyond the fundamental frequency there are higher harmonic waves generated, as is evident in the disruption of the wave ridges traveling down-wave.

The time signal and power spectral density (PSD) for the resulting wave field at $x = \pm 3\lambda_{Airy}$ are shown in Fig. 4, where T is the WEC period and T_W is the period of each generated wave. The amplitude of the fundamental wave of period $T_W/T = 1$ is the most dominant peak in the PSD plot. The down-wave flow field also features a peak of about half the magnitude of the fundamental wave at $T_W/T = 0.5$, which is responsible for the disruption in the wave ridges shown in Fig. 3. To evaluate the performance of the cycloidal WECs, the fundamental and harmonic wave heights determined from the PSD analysis are used.

To determine the effect of varying the cycloidal WEC radius on the resulting wave patterns, simulations were completed with constant circulation $\Gamma T/\lambda^2_{Airy} = 5.6 \times 10^{-3}$, and minimum submergence $|y_c + R|/\lambda_{Airy} = 0.015$. These results are shown in Fig. 5, where $H_{1,2,3}$ and $H_{-1,-2,-3}$ are the wave heights of the fundamental and next two harmonic waves traveling in the down- and up-wave directions respectively. Wave amplitudes are based on PSD analysis at $x = \pm 3\lambda_{Airy}$, initiated at $t/T = 30$ after the start of the WEC. Also shown are the corresponding powers for each wave $P_{1,2,3,-1,-2,-3}$, which have been normalized by the maximum
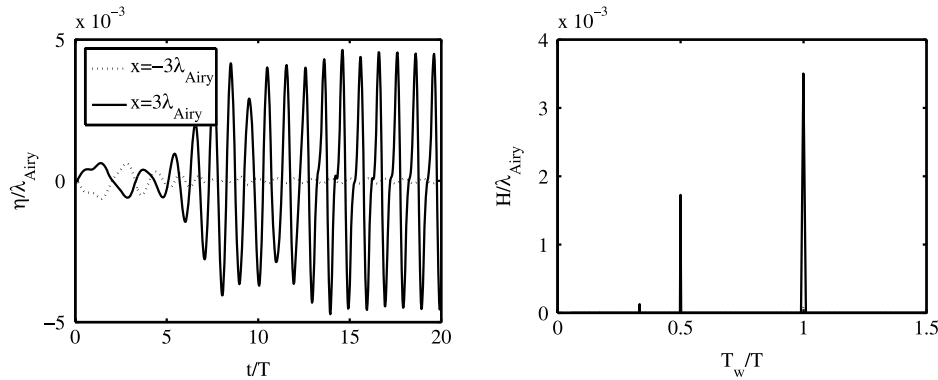
Fig. 4. Surface elevation (left) and power spectral density (right) for a cycloidal WEC of size $2R/\lambda_{Airy} = 0.3$, submergence depth $|y_c|/\lambda_{Airy} = 0.18$, and circulation $\Gamma T/\lambda_{Airy}^2 = 5.6 \times 10^{-3}$. All waves are evaluated at $x = \pm 3\lambda_{Airy}$ and time $t/T = 30$ after the start of the cycloidal WEC.
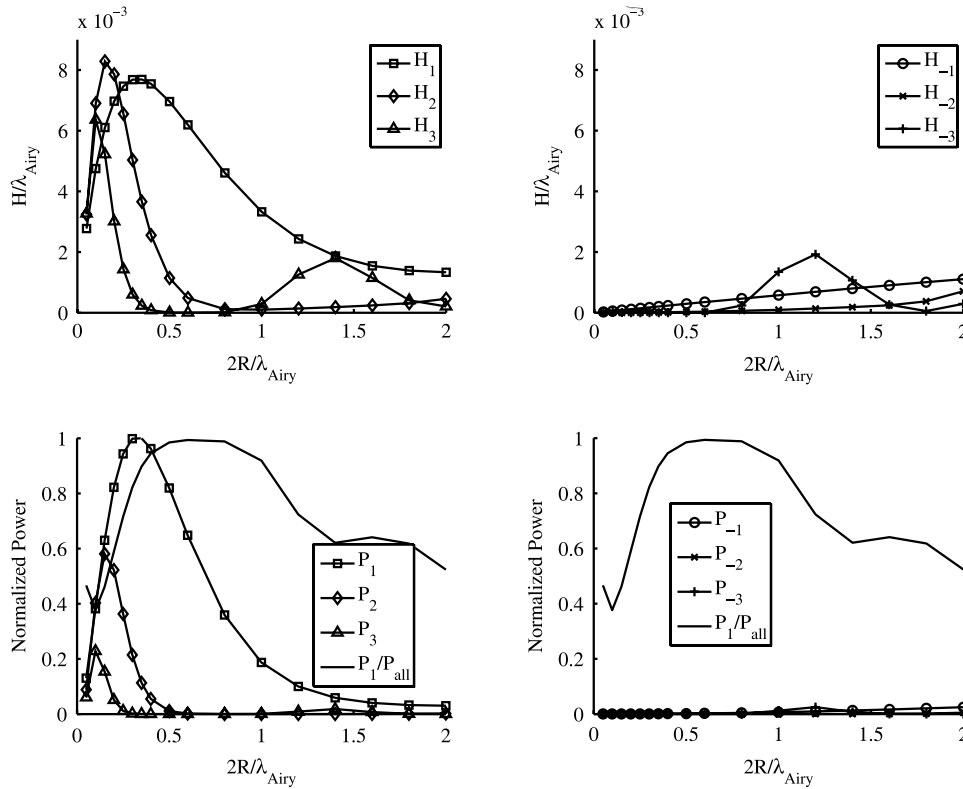

Fig. 5. Wave height (top) and power (bottom) as a function of device size for a minimum submergence $|y_c + R|/\lambda_{Airy} = 0.015$ and circulation $\Gamma T/\lambda_{Airy}^2 = 5.6 \times 10^{-3}$. All waves are evaluated at $x = \pm 3\lambda_{Airy}$ and $t/T = 30$ after the start of the cycloidal WEC.

power of the down-wave traveling fundamental wave, P_{1max}. Inspection of the down-wave traveling wave heights reveals maxima for all three waves when the hydrofoil speed and resulting wave speed are equal (i.e., $\omega R = C$ assuming Airy wave theory). For the fundamental wave this corresponds with $2R/\lambda_{Airy} = 1/\pi$, which is the optimal device size for wave generation. It is also important to note that the amplitude of the second and third harmonic waves is significant with maximum values similar to the fundamental harmonic. As a result, the optimal efficiency does not coincide with the optimal device size for wave generation and has a relatively limited bandwith with power ratios near unity for $0.5 \leq 2R/\lambda_{Airy} \leq 0.75$.
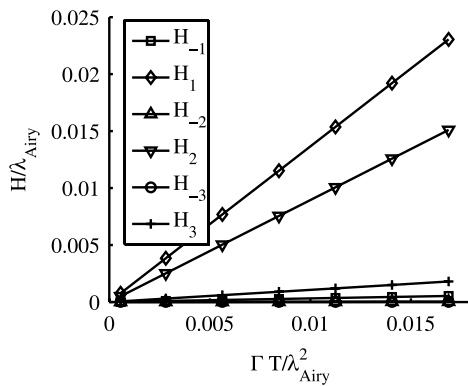
To determine the effect of submergence depth on the resulting wave field, the previous analysis was repeated for a constant device size of $2R/\lambda_{Airy} = 0.30$ and circulation $\Gamma T/\lambda_{Airy}^2 = 5.6 \times 10^{-3}$, with varying submergence depth $|y_c|/\lambda_{Airy}$. Resulting wave amplitudes and corresponding powers are shown in Fig. 6. All down-wave traveling waves show decreasing amplitudes with increasing

submergence depth. But importantly, the second and third harmonic down-wave amplitudes decrease at much faster rates then the fundamental harmonic. As a consequence, the power ratio improves with increasing submergence depth and asymptotically reaches a value of one at $|y_c|/\lambda \geq 0.255$. However, for this submergence the fundamental down-wave amplitude has decreased by more than 40% and the corresponding power has decreased by approximately 65%.

The prescribed circulation affects the necessary hydrofoil size and/or angle of attack. The previous results were obtained for a constant vortex circulation of $\Gamma T/\lambda_{Airy}^2 = 5.6 \times 10^{-3}$, and the influence of varying Γ on the resulting wave amplitudes is shown in Fig. 7. The resulting wave heights scale linearly with Γ and this applies equally to all waves generated. This behavior is expected based on inspection of the governing equation (5), but has important implications for wave cancellation. Since a linear change in circulation causes a linear change in wave amplitude, the wave
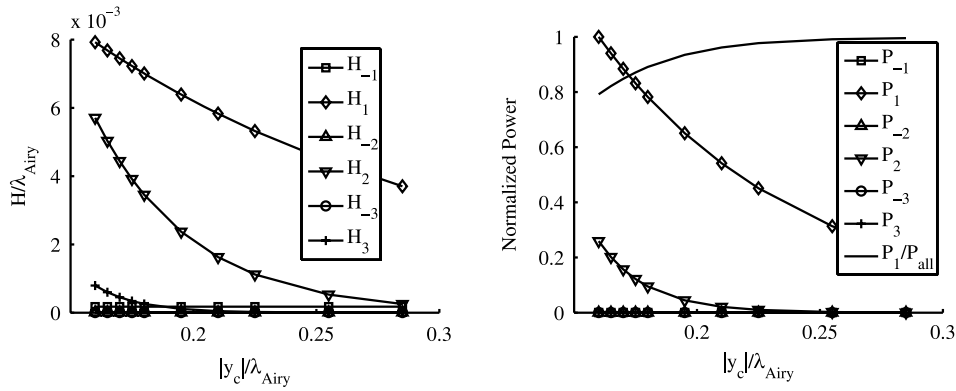
Fig. 6. Wave height (left) and power (right) as a function of submergence depth $|y_c|/\lambda_{Airy}$ for a device size $2R/\lambda = 0.30$ and circulation $\Gamma T/\lambda_{Airy}^2 = 5.6 \times 10^{-3}$. All waves are evaluated at $\pm 3\lambda$ and $t/T = 30$ after the start of the cycloidal WEC.

Fig. 7. Wave heights as a function of circulation Γ.

Fig. 8. Superposition of waves from two vortices with equal and opposite circulation and 180° of phase shift. Waves are evaluated at $x = 3\lambda_{Airy}$ for a WEC with device size $2R/\lambda_{Airy} = 0.3$, submergence depth $|y_c|/\lambda_{Airy} = 0.18$ and circulation $\Gamma T/\lambda_{Airy}^2 = \pm 5.6 \times 10^{-3}$.

energy converter can be easily adjusted to different wave heights by changing the circulation. Physically, this can be accomplished by adjusting the hydrofoil pitch and will not cause any change in conversion efficiency because all waves are scaled equally.

While the results presented so far clearly demonstrate the feasibility of using a cycloidal turbine to create a single direction traveling wave suitable for wave cancellation, the optimal design size determined by the bandwidth of the peak power ratio poses real world engineering problems when canceling deep ocean waves with wave lengths of the order of 100 m. This design challenge is addressed by improving the power ratio for smaller device sizes by considering a WEC with multiple hydrofoils.

3.2.2. Multi-blade wave energy converter

Using the theory of superposition is it possible to represent a multi-bladed cycloidal WEC. Results are shown in this section for simulations with two vortices (each representing an individual hydrofoil) of equal but opposite circulation and spaced 180° apart. The exact configuration is shown in the sketch of Fig. 1.

Plotted in Fig. 8 are the resulting wave patterns at $x = 3\lambda_{Airy}$ for a muti-blade WEC with a device size $2R/\lambda_{Airy} = 0.3$, submergence depth $|y_c|/\lambda_{Airy} = 0.18$ and circulation $\Gamma T/\lambda_{Airy}^2 = \pm 5.6 \times 10^{-3}$. The fundamental wave amplitudes from each vortex combine to produce a wave with twice the amplitude of each vortex separately. More importantly, the second harmonic waves from each vortex cancel. Inspection of the phase spectra (not shown) indicates that these waves are exactly out of phase; consequently, no second harmonic waves are present in the total wave field.

The impact of the two-blade arrangement on the power ratio and generated wave heights as a function of device size is shown in Fig. 9. The power ratio distribution is now near unity for
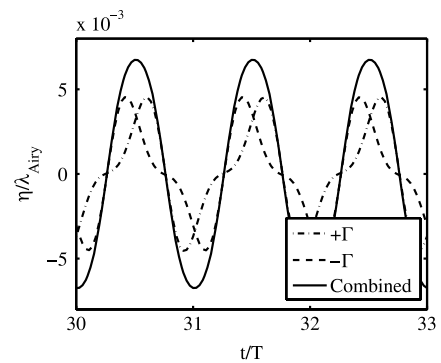
device sizes ranging from $0.2 \leq 2R/\lambda_{Airy} \leq 1.0$. For example, at $2R/\lambda_{Airy} = 0.20$ the power ratio has been increased from 0.60 for the single-blade arrangement with similar input parameters (i.e., Fig. 5) to 0.94 for the two-blade arrangement.

The results presented in Fig. 9 can also be used to determine the range of wave lengths or, conversely, wave periods for which a wave energy converter of a fixed size is able to interact efficiently with incoming waves. Since the power ratio is now flat and close to unity for device size ranging from $0.2 \leq 2R/\lambda \leq 1.0$, one could, for example, design a WEC of this type to efficiently interact with waves that differ in wave length by approximately a factor of five. For example, a WEC with $R = 20$ m can efficiently interact with wave lengths between 40 m $\leq \lambda \leq 200$ m, which is typical of deep ocean waves. While the WEC will still be able to extract a portion of the energy for waves outside of this design range, the efficiency will be reduced. This dynamic range should suffice for most wave climates found in actual deep ocean settings, negating the need to design a WEC with a variable radius which, while feasible, would add complexity to the design.

Fig. 10 shows the resulting wave heights and the corresponding wave powers as a function of submergence depth for the fundamental and harmonic waves traveling in both the up- and down-wave directions. While the decrease in fundamental wave amplitude is similar to that observed in the single vortex case shown in Fig. 6, the power ratio is now flat and close to unity for all submergence depths. This is due to the lack of any significant harmonic waves traveling in either direction; the only harmonic of detectable amplitude is the wave H_3, which does not carry any significant energy. Most notable is the absence of the second harmonic wave H_2.
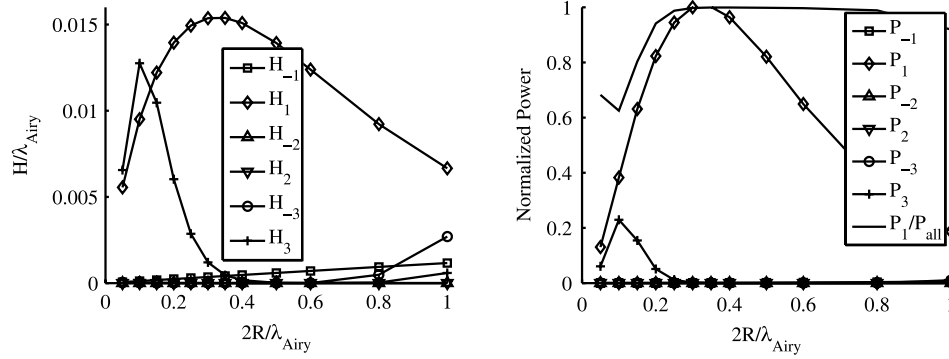
Fig. 9. Wave height (left) and power (right) as a function of device size $2R/\lambda_{Airy}$ for a two-bladed WEC with 180° of phase shift with circulation $\Gamma T/\lambda_{Airy}^2 = \pm 5.6 \times 10^{-3}$ and minimum submergence $|y_c + R|/\lambda_{Airy} = 0.015$. All waves are evaluated at $x = \pm 3\lambda_{Airy}$ at time $t/T = 30$ after the start of the cycloidal WEC.
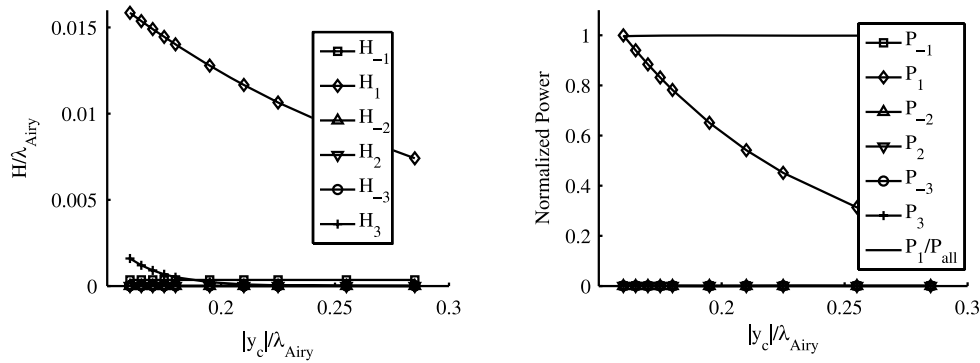
Fig. 10. Wave height (left) and power (right) as a function of submergence depth $|y_c|/\lambda_{Airy}$ for a two-bladed WEC modeled at two point vortices with 180° of phase shift for a device size $2R/\lambda_{Airy} = 0.30$ and circulation $\Gamma T/\lambda_{Airy}^2 = \pm 5.6 \times 10^{-3}$. All waves are evaluated at $x = \pm 3\lambda_{Airy}$ at time $t/T = 30$ after the start of the cycloidal WEC.

3.2.3. Wave cancellation

Superposition is used to investigate the interaction between a multi-blade WEC and an incoming Airy wave. To achieve wave cancellation, the wave generated by the WEC needs to match the incoming wave amplitude and period, while being exactly out of phase. The following linear feedback laws achieve this:

$$\delta(t) = \omega t + \theta$$
$$\Gamma = k_\Gamma H_{Airy}, \tag{12}$$

where $\delta(t)$ is the angle of the cycloidal WEC main shaft, and θ is a constant phase shift between the wave motion and the WEC rotational angle. The fixed amplitude feedback gain k_Γ is adjusted such that the amplitude of the fundamental wave H_1 created by the WEC matches that of the incoming Airy wave exactly.

Results for a WEC of device size $2R/\lambda_{Airy} = 0.3$, minimum submergence depth $|y_c + R|/\lambda_{Airy} = 0.015$ and circulation $\Gamma T/\lambda_{Airy}^2 = \pm 5.6 \times 10^{-3}$, interacting with an incoming Airy wave of period $T = 9$ s and wave height $H_{Airy} = 1.98$ m are shown in Figs. 11 and 12. The incoming wave height was empirically matched to be equal to the generated wave height, resulting in $k_\Gamma = 5.05$. Fig. 11 demonstrates the impact of phase shift between the incoming wave and the WEC rotational angle on the resulting wave field. Wave heights for the fundamental waves traveling in the up- and down-wave directions, H_1 and H_{-1}, and the down-wave harmonic H_3 are plotted separately as a function of θ. Note that these are the only waves of any significant amplitude present in the combined wave field. The optimal phase, $\theta = 10°$, corresponds to a fundamental down-wave height $H_1 = 0$, indicating that all of the incoming wave has been canceled by the WEC. The down-wave fundamental amplitude shows a strong linear relationship for feedback phases above and below the optimal angle, while there there is very little impact on H_{-1} and H_3. Thus, small phase shifts will cause major
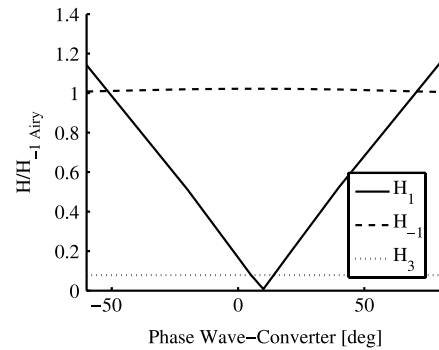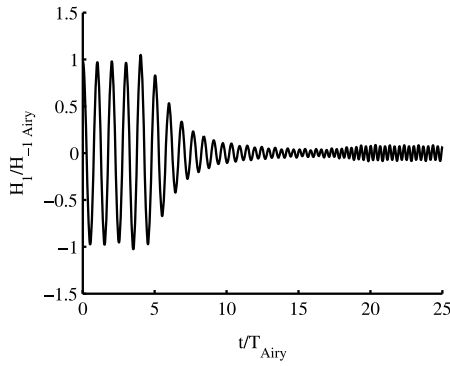

Fig. 11. Wave heights versus wave phase for a multi-bladed WEC with device size $2R/\lambda_{Airy} = 0.3$, minimum submergence depth $|y_c + R|/\lambda_{Airy} = 0.015$ and circulation $\Gamma T/\lambda_{Airy}^2 = \pm 5.6 \times 10^{-3}$, and an incoming Airy wave with period $T = 9$ s and wave height $H_{Airy} = 1.98$ m. All waves are evaluated at $x = \pm 3\lambda_{Airy}$ at time $t/T = 30$ after the start of the cycloidal wave energy converter.

losses in conversion efficiency making a phase-locked feedback system mandatory for efficient conversion. The resulting down-wave surface elevation at $x = 3\lambda_{Airy}$ as a function of time is shown in Fig. 12 for the optimal feedback phase $\theta = 10°$. After 15 revolutions of the WEC the fundamental down-wave amplitude is approximately zero, but higher harmonic waves (most prominently H_3) are still present.

3.3. Thin hydrofoil model results

While simulation with hydrofoils modeled as single point vortices provides far-field estimates of the wave field created by the cycloidal WEC, a detailed investigation of the flow field near the hydrofoils is not possible. To estimate near-field properties, such

Fig. 12. Surface elevation at $x = 3\lambda_{Airy}$ for a feedback phase of $\theta = 10°$ between a multi-bladed WEC with device size $2R/\lambda_{Airy} = 0.3$, minimum submergence depth $|y_c + R|/\lambda_{Airy} = 0.015$ and circulation $\Gamma T/\lambda_{Airy}^2 = \pm 5.6 \times 10^{-3}$, and an incoming Airy wave with period $T = 9$ s and wave height $H_{Airy} = 1.98$ m.
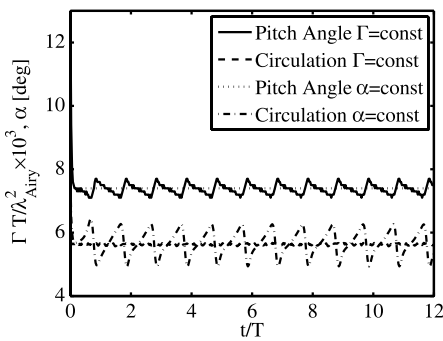
Fig. 13. Pitch angle and circulation for thin hydrofoil simulations. The hydrofoil has a chord $c/\lambda_{Airy} = 0.03$, device size $2R/\lambda_{Airy} = 0.5$, and minimum submergence $|y_c + R|/\lambda_{Airy} = 0.03$. For the constant circulation simulation $\Gamma T/\lambda_{Airy}^2 = 5.6 \times 10^{-3}$ and for the constant pitch simulation $\alpha = 7.4°$.

as hydrofoil pitch angles and chord length, the hydrofoil must be modeled using a vortex panel distribution.

3.3.1. Wave generation

An important initial step to validate the thin hydrofoil panel code is to compare far-field wave patterns created by the vortex panel simulations to the results obtained from single vortex simulations. When the hydrofoil chord is small relative to the fundamental wave length (i.e., $c/\lambda_{Airy} \ll 1$), the results from both simulations are identical.

An advantage of the vortex panel simulations is that hydrofoil pitch cycles necessary to obtain the desired circulation can be estimated. Plotted in Fig. 13 is the resulting pitch cycle for a constant circulation simulation for a hydrofoil with a chord $c/\lambda_{Airy} = 0.003$, device size $2R/\lambda_{Airy} = 0.5$, minimum submergence $|y_c + R|/\lambda_{Airy} = 0.03$, and circulation $\Gamma T/\lambda_{Airy}^2 = 5.6 \times 10^{-3}$. The resulting mean pitch angle is $\alpha = 7.4°$ with maximum variations over one cycle of less than $\pm 0.5°$. This indicates that the wave-induced flow direction and magnitude do not vary significantly as the hydrofoil travels on its circular path. Also plotted in Fig. 13 is the circulation variation when the pitch angle is held constant at $\alpha = 7.4°$. The resulting mean circulation is $\Gamma T/\lambda_{Airy}^2 = 5.6 \times 10^{-3}$ with maximum variations of $\pm 5.6 \times 10^{-4}$. These circulation fluctuations increase the fundamental wave amplitude traveling up-wave, reducing the maximum efficiency of the WEC. Thus, precise feed-back pitch control is necessary to achieve maximum WEC efficiency.

Modeling the cycloidal WEC blades as thin hydrofoils also allows one to investigate the impact of hydrofoil chord length on the generated wave field. Plotted in Fig. 14 is the variation of
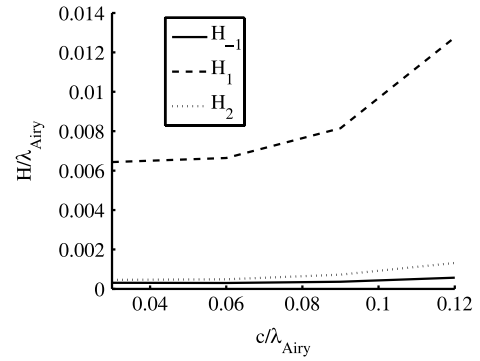
Fig. 14. Impact of chord length on wave generation. Wave amplitudes are evaluated at $x = \pm 3\lambda_{Airy}$ for a WEC with device size $2R/\lambda_{Airy} = 0.5$, minimum submergence $|y_c + R|/\lambda_{Airy} = 0.03$, and circulation $\Gamma T/\lambda_{Airy}^2 = 5.6 \times 10^{-3}$.
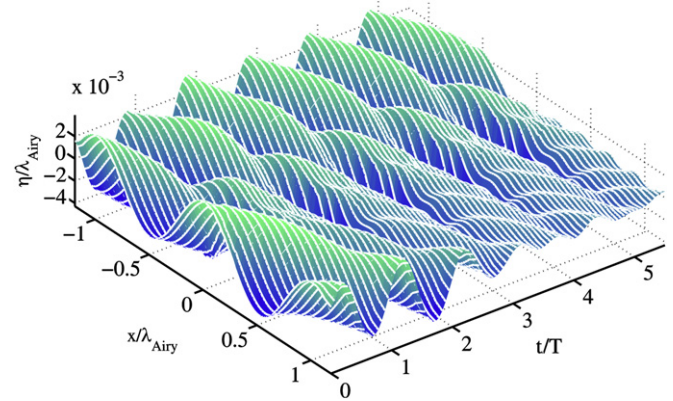
Fig. 15. Water surface–time plot for wave cancellation of an incoming Airy wave with period $T = 9$ s and wave height $H_{Airy} = 0.8$ m using a single-blade WEC modeled as a vortex panel distribution with device size $2R/\lambda_{Airy} = 0.5$, minimum submergence $|y_c + R|/\lambda_{Airy} = 0.03$, circulation $\Gamma T/\lambda_{Airy}^2 = 5.6 \times 10^{-3}$, and chord $c/\lambda_{Airy} = 0.03$.

wave amplitude with hydrofoil chord for a device size $2R/\lambda_{Airy} = 0.5$, minimum submergence $|y_c + R|/\lambda_{Airy} = 0.03$, and constant circulation $\Gamma T/\lambda_{Airy}^2 = 5.6 \times 10^{-3}$. The fundamental down-wave amplitude, H_1, increases nonlinearly with increasing hydrofoil chord, while the down-wave harmonic, H_2, and fundamental up-wave harmonic, H_{-1}, remain nearly constant. This increase in wave height is attributed to the fact that a larger hydrofoil near the surface will more effectively alter the surface elevation and thus generate a larger wave for a given circulation. This is a general sizing trend that has been observed for pressure force or buoyancy driven WECs and is reported in the literature, see for example [21]. It also applies to the hydrofoil-based wave energy conversion, both in terms of the overall converter size investigated in the previous sections, but also as seen in Fig. 14 for the hydrofoil chord length.

3.3.2. Wave cancellation

Linear superposition is again applied to investigate the interactions of the incoming Airy wave and a single-blade WEC modeled as a thin hydrofoil. Plotted in Fig. 15 is the resulting wave pattern as a function of space and time for a single-blade WEC of size $2R/\lambda_{Airy} = 0.5$, minimum submergence $|y_c + R|/\lambda_{Airy} = 0.03$, circulation $\Gamma T/\lambda_{Airy}^2 = 5.6 \times 10^{-3}$ and chord $c/\lambda = 0.03$, and an incoming Airy wave of period $T = 9$ s and wave height $H_{Airy} = 0.8$ m. Up-wave of the converter the incoming wave amplitude is unchanged at all times, indicating that no waves of any significant amplitude were generated by the WEC in the up-wave direction that interfere destructively with the incoming wave. Down-wave of the converter, the incoming Airy
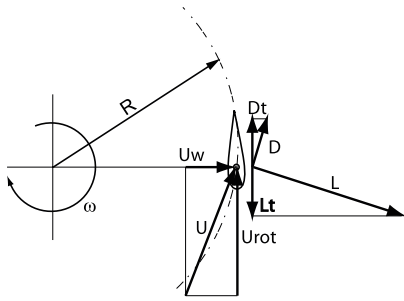
Fig. 16. Flow geometry and hydrodynamic forces.

wave is entirely canceled by the WEC's fundamental harmonic, H_1. However, as expected, because only a single-blade converter is considered, higher harmonic waves (most prominently H_2) are still present. Importantly, an investigation of the velocity field in the vicinity of the hydrofoil showed that the blade inflow velocity remained relatively constant throughout the trajectory. Thus, by operating the cycloidal WEC in sync with the incoming wave the fluctuating velocity field is rectified to achieve an almost constant inflow at the blade. From a two-dimensional perspective, the blade experiences both velocity and force components that are steady in time. Consequently, the torque and shaft power produced are also constant in time, which is an important consideration for generator design.

3.3.3. Hydrofoil sizing and impact of flow viscosity

The previous section demonstrated that for a typical cycloidal WEC operating at a fixed phase relative to an incoming wave, the wave-induced flow velocity magnitude and direction are relatively constant with respect to the hydrofoil. This finding is used to develop a first principles estimate of the effect that viscosity has on device performance.

Fig. 16 shows the induced velocity components and the resulting hydrodynamic lift and drag forces. The wave-induced flow velocity U_W is assumed have constant magnitude and is oriented radially outward as the hydrofoil rotates. As illustrated in Fig. 16, the component of lift force tangential to the path of the hydrofoil, L_T, is responsible for the production of torque and thus shaft power, while the tangential drag force, D_T, acts to reduce the shaft torque. Thus the viscous losses can be estimated by the ratio of D_T/L_T, which is a function of the lift to drag force ratio, wave velocity U_W, and hydrofoil rotational velocity U_{rot} according to $D_T/L_T = D/L(U_{rot}/U_W)$. It is immediately evident that as the speed ratio U_{rot}/U_W is increased the lift vector becomes more aligned with the radial direction and thus the tangential component of the lift vector is decreased. In addition, the tangential component of drag increases. However, for small speed ratios the lift produced is reduced quadratically to the relative flow speed U, even though the geometric conditions for torque production are improved.

4. Dimensional results

While the performance of the cycloidal wave energy in non-dimensional quantities was presented throughout this text, it is helpful to report at least one typical design result in dimensional form. For this we will consider the North Atlantic wave introduced in Section 3 (i.e., $T = 9$ s) with wave height $H = 3.5$ m and energy $P_{Airy} = 108$ kW m^{-1}. For such an incoming wave the optimal device size is $R \approx 20$ m, and the incoming wave is entirely canceled using two hydrofoils each producing a constant circulation of $\Gamma \approx 17$ m^2/s. Assuming a realistic lift coefficient of $c_l = 0.75$, a hydrofoil chord of $c \approx 3.25$ m is required to achieve this circulation. The induced velocity ratio is $U_{rot}/U_W \approx 11$; thus, assuming a lift to drag ratio $L/D = 40$ yields an estimate of the tangential drag

to lift ratio $D_T/L_T \approx 0.275$, indicating that just under 30% of the wave energy is lost to hydrofoil drag. Consequently, an estimate of the available shaft power would be $P_s \approx 77$ kW m^{-1}, and a blade span of only $S = 13$ m would thus yield 1 MW of shaft power after subtracting the viscous losses.

5. Conclusions

The well known cycloidal turbine can be used both as an efficient wave maker, as well as a wave termination device when synchronized to an incoming wave by means of feedback control. Inviscid two-dimensional simulation results for cycloidal WECs featuring both a single hydrofoil as well as two hydrofoils spaced 180° apart are presented. The hydrofoils of the WEC are modeled either as a point vortex, or as a thin hydrofoil using a vortex panel distribution. Both simulations capture the waves produced in the far-field with good accuracy. However, thin hydrofoil simulations enable the investigation of necessary pitch control schemes and hydrofoil chord length.

5.1. Wave generation

For wave generation, it is possible to create a single Airy type wave that only travels in one direction, with no wave being generated in the other direction. The direction of travel is controlled by the rotation direction, while the wave height varies linearly with hydrofoil circulation. For a single-blade WEC the resulting wave field was decomposed into the fundamental wave traveling up-wave and two higher harmonics traveling both up- and down-wave. The optimal device radius was determined to be $2R/\lambda_{Airy} = 1/\pi$, corresponding to an exact match between the hydrofoil rotational velocity and the wave speed of the generated wave. A significant improvement in the wave field was achieved using a WEC with two hydrofoils spaced 180° apart with equal but opposite circulation. For this configuration, the harmonic wave of twice the fundamental frequency was reduced to negligible amplitudes, resulting in a significantly improved wave field for wave termination applications.

5.2. Wave cancellation

The single-sided wave generated by the cycloidal WEC is perfectly suited to extract energy from an incoming plane Airy wave. In order to achieve this, the motion of the WEC needs to be synchronized in frequency and phase locked to the incoming wave, and the circulation of the converter's hydrofoils needs to be adjusted to produce a wave of matching amplitude by means of feedback flow control. If this is accomplished, in the two-dimensional inviscid limit, more than 99% of the incoming wave energy can be extracted from the wave achieving wave termination. The hydrofoil in this situation experiences an almost constant inflow throughout the rotation of the converter, resulting in almost constant torque and thus shaft power. The WEC thus functions as a fluid dynamic rectification device when considering the moving reference frame of the rotating hydrofoil, while the reactive force at the main shaft is changing direction through 360° for each revolution.

References

[1] Boyle G. Renewable energy—power for a sustainable future. Oxford University Press; 2004.

[2] Bedart R. Final summary report — offshore wave power feasibility demonstration project. TechRep. E2I EPRI Global. WP 009 — US Rev 1; 2005.

[3] Evans DV. A theory for wave-power absorption by oscillating bodies. J Fluid Mech 1976;77(1):1–25.

[4] Betz A. Das maximum der theoretisch möglichen ausnützung des windes durch windmotoren. Zeitschrift für das gesamte Turbinenwesen 1920;26:307–9.

[5] McCormick M. Ocean wave energy conversion. John Wiley & Sons; 1981.

[6] Mei CC. The applied dynamics of ocean surface waves. New York: John Wiley & Sons; 1983.

[7] Cruz J. Ocean wave energy: current status and future prepectives. Springer-Verlag; 2008.

[8] Wu TYT. Swimming of a waving plate. J Fluid Mech 1961;10:321–44.

[9] Grue J, Mo A, Palm E. Propulsion of a foil moving in water waves. J Fluid Mech 1988;186:393–417.

[10] Isshiki H. A theory of wave devouring propulsion (1st report). Thrust generation by a linear wells turbine. J Soc Nav Arch Japan 1982;151:54.

[11] Isshiki H, Murakami M. A theory of wave devouring propulsion (3rd report). An experimental verification of thrust generation by a passive-type hydrofoil propulsor. J Soc Nav Arch Japan 1983;154:125.

[12] Isshiki H, Murakami M, Terao Y. Utilization of wave energy into propulsion of ships — wave devouring propulsion. In: Naval hydrodynamics; 1985.

[13] Terao Y. Wave devouring propulsion system from concept to trans-pacific voyage. In: Proceedings of the 28th international conference on ocean, offshore and arctic engineering. ASME; 2009.

[14] Marburg C. Investigation on a rotating foil for wave energy conversion. Master's thesis; TU Delft; 1994.

[15] van Sabben E. De in het snelheidsveld van lopende golven ronddraaiende plaat; invloed op het vrije vloeistofoppervlak. Master's thesis. TU Delft; 1987.

[16] Hermans AJ, van Sabben E, Pinkster J. A device to extract energy from water waves. Appl Ocean Res Comput Mech Publications 1990;12(4):5.

[17] Pinkster J, Hermans AJ. A rotating wing for the generation of energy from waves. In: 22nd IWWWFB conference. Plitvice (Croatia); 2007.

[18] Newman JN. Marine hydrodynamics. MIT Press; 1977.

[19] Wehausen J, Laitone E. Surface waves, handbook of physics, vol. 9. Springer-Verlag; 1960.

[20] Katz J, Plotkin A. Low-speed aerodynamics. 2nd ed. Cambridge University Press; 2001.

[21] Falnes J. Ocean waves and oscillating systems. Cambridge University Press; 2002.